Analyst

PAPER

View Article Online
View Journal | View Issue

Cite this: *Analyst*, 2026, **151**, 478

Single-molecule nanopore profiling of protein domain fragment dynamics and aggregation

Dapeng Chen,†[a,c] Fei Zheng,*†[b] Guangle Qin,[a,c] Chaofan Ma,[a] Wei Liu,[a] Lichun Zou,[a] Haiyan Wang[a] and Jingjie Sha*[a]

Protein fragmentation offers an effective approach for resolving localized conformational information and mapping discrete structural domains, yet current techniques may miss their dynamic behavior under changing external environments. Here, we harness nanopore sensing to interrogate 50-residue fragments from N-terminal (NTD) and C-terminal domains (CTD) of the SARS-CoV-2 nucleocapsid (N) protein under physiological conditions. We propose utilizing fractional current blockade ($\Delta I/I_0$) as a metric for the conformational spectrum, enabling us to probe the dynamics and aggregation behavior of protein fragments across various conditions. By systematically varying the voltage (70–300 mV) and employing complementary molecular dynamics simulations, we observe significant alterations in $\Delta I/I_0$ and translocation duration (τ), which indicate distinct domain-specific behaviors. Notably, the CTD fragment exhibits dimerization at lower voltages, followed by dissociation at elevated voltages, thus highlighting the capability of nanopore assays to resolve dynamic single-molecule transitions in real time. Additionally, we elucidate the electric field-dependent dimer dissociation behavior using size-variant nanopores and artificially modulate the environment of the CTD fragments to explore the factors affecting fragment dimerization. The full width at half maximum (FWHM) of the fitted conformational spectrum is employed to assess protein conformational flexibility and stability, influenced by voltage and ionic strength. Our findings not only reveal electric field-driven conformational plasticity of N-protein but also advance nanopore-based strategies for real-time protein domain analysis, informing antiviral therapeutic and diagnostic development.

Received 28th October 2025,
Accepted 2nd December 2025

DOI: 10.1039/d5an01140j

rsc.li/analyst

Introduction

Proteins play central roles in biological systems, executing a vast array of functions essential for life. Investigating a protein in its entirety can be complex, especially when crucial functional or structural information is hidden within certain domains or motifs.[1–3] Consequently, fragmentation by limited proteolysis or synthetic expression is commonly used in structural studies to analyze the conformational and functional properties of protein domains.[4,5] Mass spectrometry (MS) and nuclear magnetic resonance (NMR) spectroscopy have each contributed significantly to advances in structural biology.[6,7] However, both techniques present specific challenges. For example, high-sensitivity MS often relies on ionization conditions that differ from native biological environments, which can affect the preservation of structural features.[8] Similarly, NMR offers atomic-level conformational detail but generally requires relatively large amounts of purified protein and lengthy acquisition times, which can limit its suitability for dynamic or low-abundance systems.[7,9] These windows motivate alternative single-molecule approaches.

Solid-state nanopores furnish such an alternative for single-molecule characterization of proteins under physiologically relevant conditions.[10–16] Nanopores enable real-time monitoring of ionic current modulations as analytes traverse the pore sensing region, delivering rich, time-resolved electrical signatures.[17–20] Moreover, nanopore assays are inherently single-molecule in nature, giving them the sensitivity to detect structural changes that might be averaged out or overlooked by ensemble techniques.[21–25] They can also discern transient conformations, making them suitable for exploring dynamic behaviors.[26,27] Another advantage lies in the ability to modulate experimental parameters—such as voltage[28] or buffer composition—*in situ*, facilitating observations of how protein fragments respond to changing external conditions.

SARS-CoV-2 nucleocapsid (N) protein represents a polyfunctional scaffold critical to the viral lifecycle, characterized by its modular architecture—the RNA-binding N-terminal domain

[a]*Jiangsu Key Laboratory for Design and Manufacture of Micro-nano Biomedical Instruments, School of Mechanical Engineering, Southeast University, Nanjing 211189, China*
[b]*Cavendish Laboratory, University of Cambridge, Cambridge CB3 0HE, UK. E-mail: fz284@cam.ac.uk, major212@seu.edu.cn*
[c]*Jiangsu Automation Research Institute, Lianyungang 222000, China*
†These authors contributed equally.

(NTD) and the oligomerization-enabling C-terminal domain (CTD).[29,30] Central to viral pathogenesis, the N protein coordinates viral genome packaging, regulates replication-transcription cycles, and mediates immune evasion. The NTD facilitates sequence-specific RNA recognition, anchoring the viral genome into compact ribonucleoprotein (RNP) assemblies. In contrast, the CTD employs a conserved dimerization interface to drive higher-order oligomerization, spatially organizing N protein subunits into stable RNP complexes.[31] Structural analyses reveal that CTD-mediated oligomerization is indispensable for viral propagation:[32,33] dimeric units polymerize *via* hydrophobic and electrostatic interfaces to form helical RNP structures that encapsulate and stabilize the RNA genome. This cooperative interplay between the NTD's RNA-binding specificity and the CTD's oligomerization-driven architecture ensures efficient viral replication and immune antagonism. By delineating these domain-specific mechanisms, the N protein emerges as a promising target for disrupting viral assembly and advancing diagnostic platforms that exploit its structural features.[34]

Here, we utilize nanopore technology to investigate two specific 50-amino-acid fragments derived from the NTD and CTD of the SARS-CoV-2 N protein. The choice of fragments is guided by two criteria: (i) each segment contains the key structures of the corresponding domain;[31] (ii) their hydrodynamic size fall within the detection range of our 10–20 nm nanopores. Importantly, we do not claim that fragments capture every aspect of full-length behavior; rather, they allow us to isolate domain-specific stability and association tendencies while avoiding the disorder-rich central linker that complicates whole-protein measurements. We propose employing the distribution of fractional current blockade ($\Delta I/I_0$) as a conformational spectrum to investigate the dynamics and aggregation behavior of protein fragments. By subjecting these fragments to varying external voltage conditions, we systematically examined their conformational dynamics at elevated voltages (200–300 mV) and their aggregation kinetics at lower voltages (70–100 mV). Key parameters, including $\Delta I/I_0$ and translocation duration (τ), were extracted from thousands of nanopore translocation events and complemented by molecular dynamics (MD) simulations. Our findings reveal that the nanopore platform is capable of detecting the dimerization of CTD-derived protein fragments (spanning 50 of 118 amino acids) and, importantly, demonstrate that these dimers dissociate under increasing voltage conditions. We further related this dissociation behavior to electric field strength *via* fragment measurements by size-variant nanopores. We demonstrate proper fragment concentration and pH environment are critical for CTD fragment dimerization. Additionally, we show that the conformational flexibility of this fragment is significantly affected by the electric field and ionic strength. These results provide insights into the structural and functional behavior of the SARS-CoV-2 N protein, while also demonstrate that nanopore technology is a promising tool for studying protein fragments, thereby facilitating the development of diagnostic strategies and targeted therapeutics.

Results and discussion

Fig. 1a illustrates the domain architecture of the SARS-CoV-2 N protein, comprising the N-arm, NTD, linker region (LKR), CTD, and C-tail. Given that the NTD and CTD are the most crucial functional domains, we exemplified two protein fragments, each consisting of 50 amino acids, derived from these two regions, with sequences spanning 14 to 63 in the NTD and 3 to 52 in the CTD, respectively. For clarity, we refer to these fragments by their corresponding PDB IDs: 7CDZ for the NTD fragment and 7CE0 for the CTD fragment. The higher-order conformational structures of these two proteins are depicted in Fig. 1b and c, respectively, with 7CDZ exhibiting a more disordered conformation, while 7CE0 is characterized by the presence of three alpha helices.

We fabricated the nanopore sensors on 10 nm-thick silicon nitride (SiN) membranes using controlled dielectric breakdown (CBD). We employed established MEMS techniques to fabricate SiN membranes suspended on a Si substrate,[35–37] sandwiching a SiO_2 layer to minimize capacitive noise. We controlled nanopore sizes through fabrication parameters, transmembrane voltage, and breakdown duration during CBD; details are provided in SI Notes S1 and S2. Fig. 1d and e illustrate the working principle of nanopore microscopy for decoding the conformational information and dynamic behavior of protein fragments. A transmembrane potential is applied across the nanopore, driving charged proteins to electrophoretically pass through it (Fig. 1d). As the target protein occupies the nanopore, there is a transient decrease in the ionic current generated by mobile ions within the nanopore. Each translocation event yields a single-molecule current signature of the protein, and the accumulation of thousands of events produces a long current trace that can be translated into a conformational spectrum, reflecting the distributions of preferred conformations for the protein (Fig. 1e).

Protein discrimination and conformational switching at high voltages

We investigated the behavior of protein fragments during nanopore translocation under high voltage conditions (200–300 mV). Fig. 2a and b depict typical 30-second current traces at 200 mV, illustrating without and in the presence of the protein fragments 7CE0 and 7CDZ, respectively. The translocation frequency of 7CDZ exceeds that of 7CE0, likely due to its larger hydrodynamic volume. Fig. 2c presents the distributions of fractional current blockade for 7CE0 and 7CDZ at both 200 mV (top panel) and 300 mV (bottom panel). At 200 mV, both protein fragments exhibit a single normal distribution; however, the average $\Delta I/I_0$ of 7CE0 (0.02) is lower than that of 7CDZ (0.025). This difference is attributable to the smaller hydrodynamic volume of 7CE0, measured at 29.3 nm^3 in MD simulations, compared to 44.3 nm^3 for 7CDZ, despite their similar molecular weights and same number of residues (Fig. S7). In contrast, at 300 mV, the $\Delta I/I_0$ distribution for 7CDZ reveals two distinct distributions, with one peak at 0.025 and another emerging at 0.034. This behavior suggests that some 7CDZ fragments are stretched by the enhanced electric

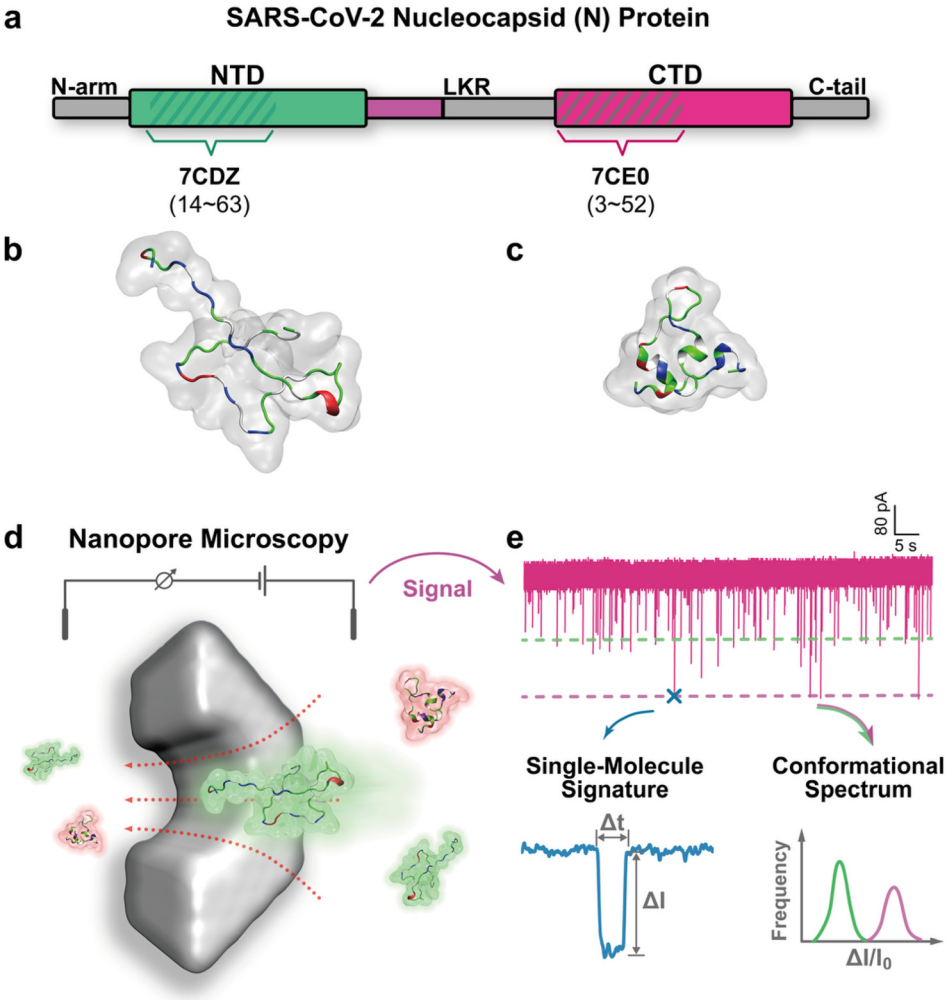

Fig. 1 SARS-CoV-2 N protein and nanopore microscopy for conformational analysis. (a) Domain architecture of the SARS-CoV-2 N protein, comprising the N-arm, NTD, LKR, CTD, and C-tail. Two protein fragments, 7CDZ (residue 14–63) and 7CE0 (residue 3–52) derived from NTD and CTD respectively are examined. (b) Structural conformation of the NTD protein fragment. (c) Structural conformation of the CTD protein fragment. (d) Schematic of nanopore microscopy, leveraging the electrophoretic translocation of protein fragments through the nanopore under a transmembrane voltage, resulting in a signal change. (e) Example of the ionic current trace obtained during nanopore translocation, depicting single-molecule signatures that contribute to the derived conformational spectrum, which indicates the distributions of protein conformations.

field and may unfold into larger conformational states. In comparison, 7CE0 fragments maintain their original conformation at elevated transmembrane voltages, likely due to their rich secondary structure (alpha helices), which confer greater conformational stability. Additionally, we examined the translocation durations of these protein fragments, which exhibited distinct patterns, as shown in Fig. 2d. We fitted the duration distributions using an exponential decay function to derive the mean translocation duration. For 7CE0, the duration decreases from 56 μs at 200 mV to 37 μs at 300 mV, consistent with expectations for electrophoretically driven translocation. Conversely, the duration of 7CDZ exhibits an increasing trend, rising from 96 μs to 119 μs, attributable to the larger size of 7CDZ and its conformational changes at higher voltages.

To elucidate the translocation dynamics of the two protein fragments, we performed MD simulations to reproduce the behavior observed in experiments. Detailed simulation parameters are outlined in Methods and Materials. Fig. 2e and f present the current values during the translocation of the protein fragments through a SiN nanopore. The average remaining current (I) for 7CDZ is 27.5 nA, which is lower than that of 7CE0 at 28.8 nA. This observation is consistent with experimental data indicating that 7CDZ occupies a larger volume within the nanopore compared to 7CE0. As observed in experiments, the translocation duration of 7CDZ (108 ns) exceeds that of 7CE0 (38 ns). The discrepancy in duration values between simulations and experiments is attributed to the necessitated high field strength to drive the fragments through the nanopore and the initial positioning of the molecules at the pore boundary, which does not account for the time required for molecules to approach from the bulk to the pore. Analysis of the simulation trajectories revealed that the

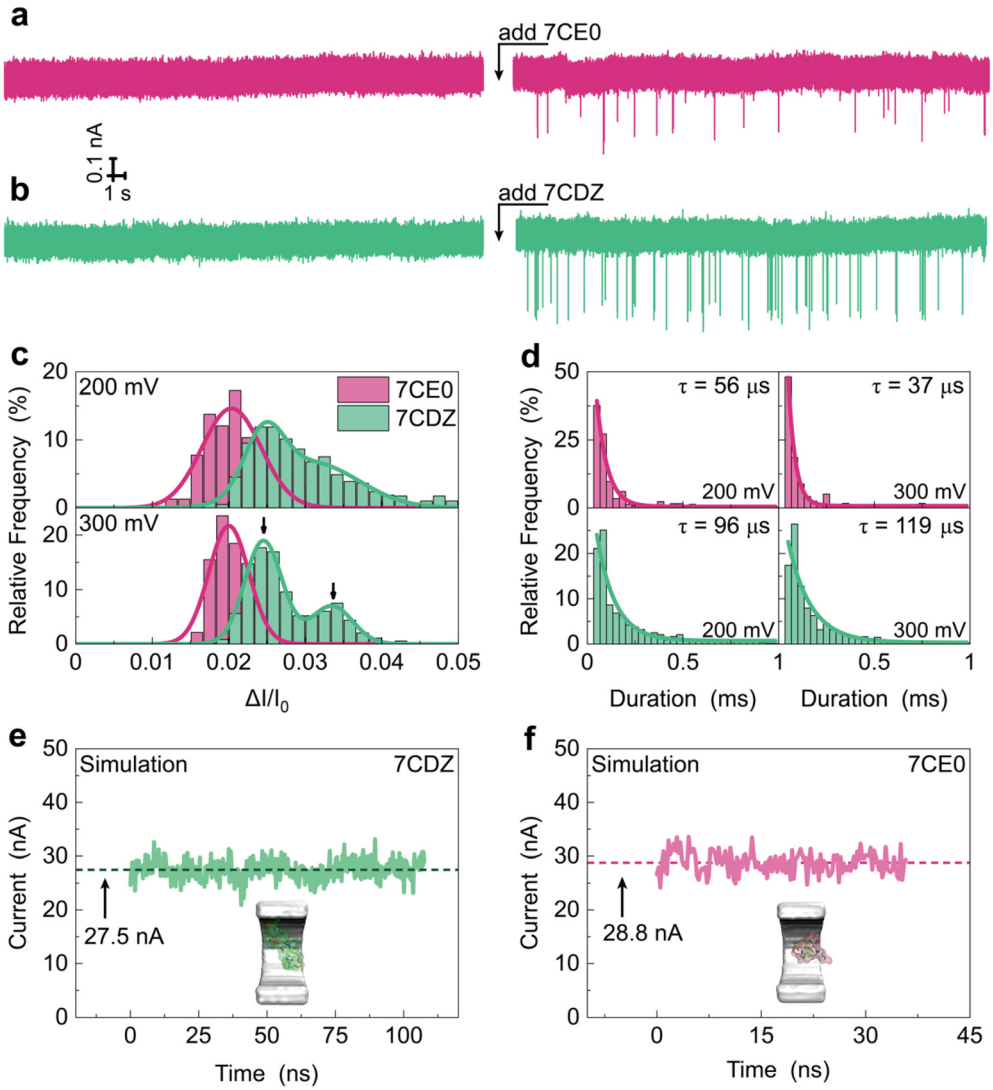

Fig. 2 Translocation dynamics of protein fragments 7CE0 and 7CDZ through a SiN nanopore under high voltage conditions. (a and b) Current traces of 30 seconds at 200 mV, for without targets (baseline) and in the presence of the protein fragments 7CE0 and 7CDZ, respectively. (c) Distributions of fractional current blockade ($\Delta I/I_0$) for 7CE0 (magenta) and 7CDZ (green) at 200 mV (top panel) and 300 mV (bottom panel). The number of events, *N*, for each condition is 300. (d) Translocation duration distributions and fitted mean durations for 7CE0 and 7CDZ at both voltages. (e and f) Current traces from MD simulations for 7CDZ and 7CE0, respectively.

7CDZ fragment interacts with the inner wall of the pore, contributing to its extended duration within the nanopore (Fig. S8).

Detection of fragment dimers and their dissociation dynamics at low voltages

We then shifted our focus to the low voltage range to investigate the conformational spectrum of protein fragments. As previously mentioned, 7CDZ originates from the RNA-binding domain (NTD), while 7CE0 is derived from the dimerization domain (CTD). Fragments in the dimerization domain play a crucial role in the dimerization and subsequent oligomerization of N protein subunits into RNP complexes. An exquisite examination of the CTD fragments utilizing nanopore sensing allows for the precise mapping of functional regions that govern dimerization behavior. Thus, we employed SiN nanopores to analyze the conformational spectrum of 7CE0 across various low voltages (70–100 mV) to explore its dimerization behavior. In contrast, 7CDZ did not exhibit any signs of dimerization and will not be included in this discussion.

Fig. 3a depicts a typical aggregation pathway for proteins, progressing from monomers to dimers, oligomers, and eventually fibrils. In our nanopore experiments with 7CE0, only the initial transition from monomers to dimers was observed. The absence of higher-order aggregation may be attributed to the structural conformation of the 7CE0 fragments, which does not support further oligomerization, or to insufficient fragment concentration. As illustrated in Fig. 3b and c, monomers and dimers traversing the nanopore exhibited distinct distributions in the conformational spectrum, characterized by

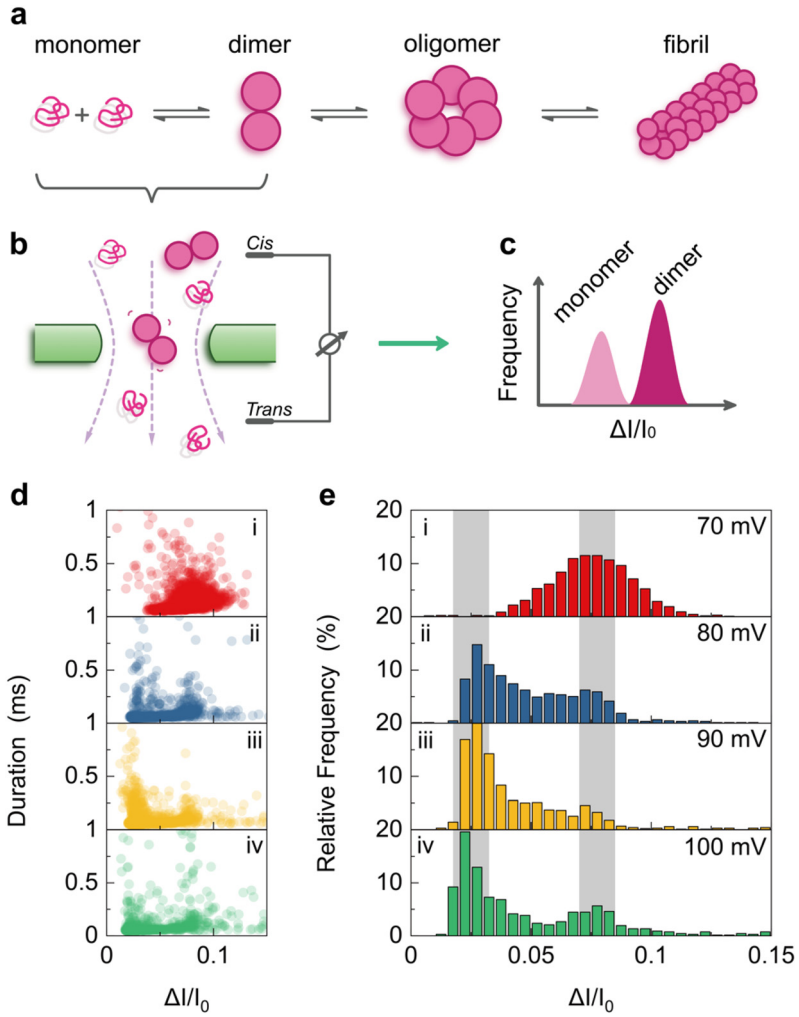

Fig. 3 Detection of 7CE0 fragment dimers and their dissociation dynamics under low voltage conditions. The nanopore diameter is 10 nm. The bulk concentration of 7CE0 fragment is 60 μM. (a) Schematic illustration of the aggregation pathway from monomers to dimers and higher-order structures. (b) Schematic illustration depicting the nanopore translocation of 7CE0 fragment monomers and dimers. (c) Conformational spectrum presenting the $\Delta I/I_0$ distribution profiles of monomers and dimers. (d) Scatter plot displaying the duration (ms) *versus* $\Delta I/I_0$ for observed transitions at varying voltages: (i) 70 mV, (ii) 80 mV, (iii) 90 mV, and (iv) 100 mV. (e) Conformational spectrum across the four voltage conditions, with the two gray shaded areas representing the distributions of monomers and dimers, respectively. The number of events, *N*, for each condition is 1000.

varying $\Delta I/I_0$ values that arise from differences in excluded volumes within the nanopore.[17] Upon translating thousands of current signatures into scatter distributions (Fig. 3d, $\Delta I/I_0$ *versus* duration) and the conformational spectrum (Fig. 3e), we noted a noteworthy shift in the $\Delta I/I_0$ distribution with increasing voltages. At 70 mV, a single normal distribution of $\Delta I/I_0$ was observed, peaking at 0.075. However, when the voltage was increased by 10 mV, the frequency of this $\Delta I/I_0$ distribution decreased, while another distribution emerged, peaking at approximately half that value (0.03). Further increases in voltage to 90 and 100 mV amplified this trend, with most detected molecules distributing around $\Delta I/I_0 = 0.04$. The fractional current blockade of biomolecules in nanopore sensing is fundamentally proportional to the excluded hydrodynamic volume, represented as $\Delta I/I_0 = V_{\text{biomolecule}}/V_{\text{nanopore}}$. Consequently, we can attribute $\Delta I/I_0 = 0.08$ to 7CE0 fragment dimers and $\Delta I/I_0 = 0.04$ to monomers. At lower voltages (70 mV), the majority of 7CE0 fragments exist in a dimeric state, and they are likely dimers at voltages below 70 mV and in a natural non-voltage environment. As the voltage is elevated, the dimers dissociate into monomers due to the electric forces acting upon them. Higher voltages (80–100 mV) facilitate this transition.

Noted that we do not observe multi-level or stepwise current signatures that would indicate dimer breakup inside the pore; representative traces for events assigned to the monomer and dimer populations instead display single-level blockades (Fig. S12). This suggests that the voltage-induced dissociation of the 7CE0 dimer occurs predominantly in the high-field capture zone at the pore entrance, where the electric field is also strong, and that the pore mainly reports on monomers and intact dimers that have already been separated by this field-driven process.

Dimer dissociation dynamics detected using size-variant nanopores

We employed size-variant nanopores to investigate the dimer dissociation behavior of 7CE0 fragments, further elucidating its dependence on the electric field. Two nanopores with diameters of 15 nm and 20 nm were selected for comparison with the previously utilized 10 nm nanopore. Fig. 4a and b present the conformational spectra of 7CE0 fragments obtained from the 15 nm and 20 nm nanopores, with the four panels arranged from top to bottom corresponding to applied voltages of 70 to 100 mV. Consistent with our findings from the 10 nm nanopore, both larger nanopores effectively monitor dimer dissociation at elevated voltages. Notably, the frequencies of monomer distributions at equivalent voltages in the 15 nm and 20 nm nanopores are lower than those observed in the 10 nm nanopore, indicating a reduced conversion rate of dimers to monomers in the larger nanopores. We quantified this phenomenon by calculating the monomer-to-dimer ratio, defined as the frequency of monomers divided by that of dimers, as illustrated in Fig. 4d. The monomer-to-dimer ratios (R) for the three size-variant nanopores adhere to the following

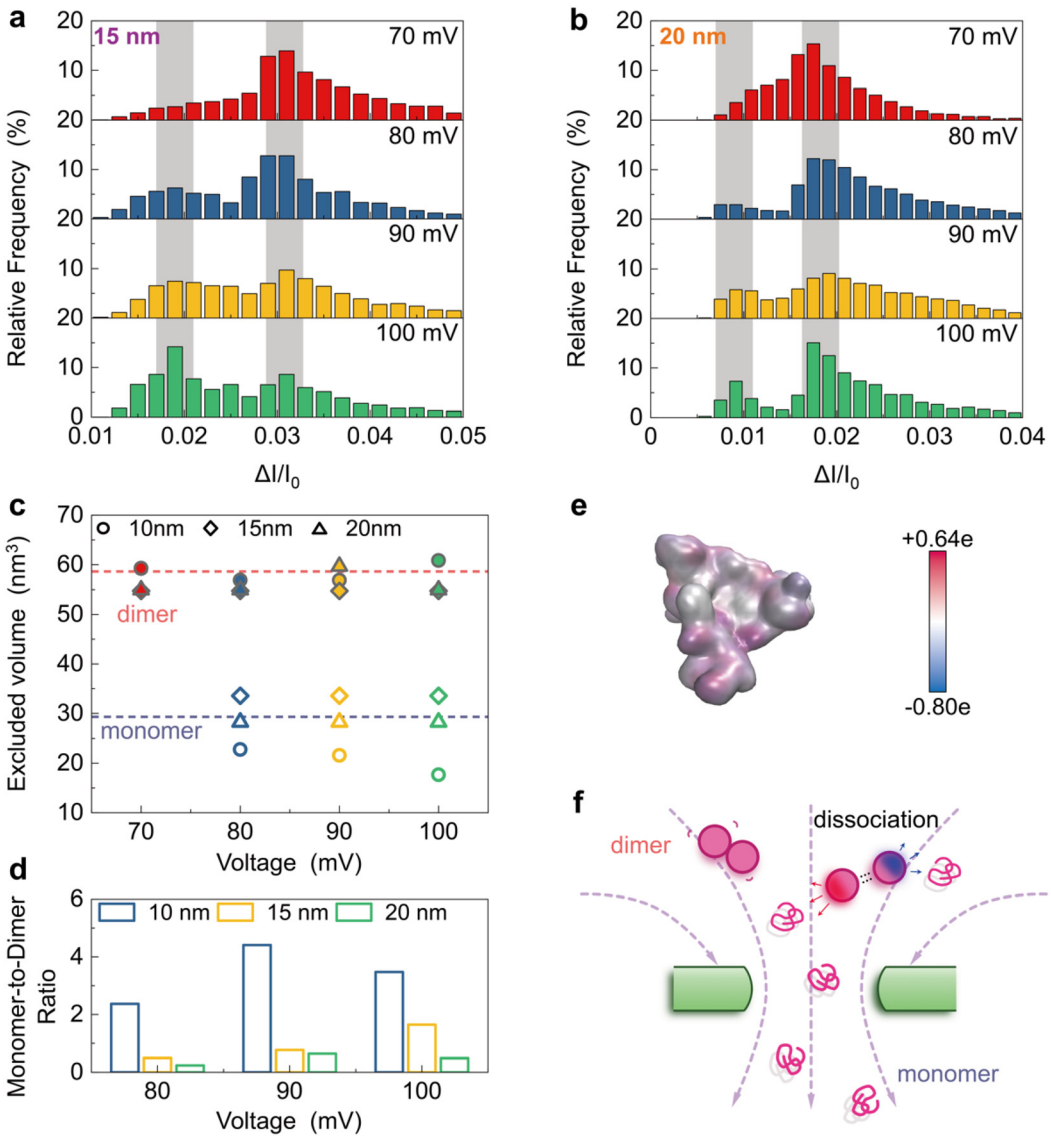

Fig. 4 Dimer dissociation behavior of 7CE0 fragments assessed using size-variant nanopores. (a and b) Conformational spectra of 7CE0 fragments from the 15 nm and 20 nm nanopores, respectively, at applied voltages ranging from 70 to 100 mV, with corresponding density plots provided in Fig. S9 and S10. The number of events, N, for each condition is 1000. (c) Excluded volumes of monomers and dimers across the three nanopore sizes, with simulation-derived values indicated by dashed lines (indigo for monomers at 29.3 nm^3 and pink for dimers at 58.6 nm^3). (d) Monomer-to-dimer ratios (R) for the three nanopore sizes at varying voltage. (e) Charge density surface profile of the 7CE0 fragment derived from MD simulations, with the range of charged residues from $-0.8e$ to $+0.64e$. (f) Schematic illustration depicting the mechanism of dimer dissociation, where localized electric forces acting on dimers facilitate the transformation of dimers into monomers at elevated voltages.

sequence: $R_{10\ nm} > R_{15\ nm} > R_{20\ nm}$. Similarly, across the varying voltage settings, the monomer-to-dimer ratios generally follow the order: $R_{100\ mV} > R_{90\ mV} > R_{80\ mV}$. After obtaining $\Delta I/I_0$ values for monomers and dimers, we calculated their excluded volumes in these three nanopores, as presented in Fig. 4c. The excluded volumes demonstrated high consistency across the three nanopores, with simulation-derived values indicated by indigo (29.3 nm^3 for monomers) and pink (58.6 nm^3 for dimers) dashed lines. This further validates the presence of 7CE0 fragment dimers and their dynamic transition to monomers at low voltages ranging from 70 to 100 mV.

To elucidate the mechanism of dimer dissociation for the 7CE0 fragment, we calculated its charge density through MD simulations and visualized the results *via* a surface profile, as shown in Fig. 4e. The 7CE0 fragment, composed of various charged residues ranging from negative ($-0.8e$) to positive ($+0.64e$), exhibits a complex charge density distribution within its structure. This variation suggests that under an external electric field, the fragment experiences localized electric forces acting in different directions. As illustrated in Fig. 4f, we hypothesize that these local forces effectively stretch the dimer,[38] facilitating its deformation into two monomers. This process may occur in the nanopore access region prior to translocation, where the electric field is sufficiently strong. As a result, a greater number of monomers are detected by the nanopore sensor at elevated voltages.

Factors influencing fragment dimerization observed using nanopores

We then modified the environmental properties of the 7CE0 fragment to determine the factors influencing dimerization. First, we reduced the bulk concentration of the 7CE0 fragment to 600 nM. The resulting conformational spectrum is presented in Fig. 5a. Across all four applied voltages, the $\Delta I/I_0$ values conform to a single normal distribution, peaking at 0.01 corresponding to the monomeric state. This difference suggests that at low concentrations of the 7CE0 fragment, the likelihood of dimerization is diminished, likely due to a reduced probability of intermolecular interactions. Furthermore, as we adjusted the solution pH from 8 to 6, the conformational spectrum continued to exhibit a singular monomeric distribution (Fig. 5b). This observation may be ascribed to alterations in both electrostatic and hydrophobic interactions among the monomers,[38] which impede the binding interface necessary for dimerization.

Conformational flexibility modulated by voltage and ionic strength

Thus far, we have utilized the $\Delta I/I_0$ distribution as a conformational spectrum to analyze the constituents of the targets through the nanopore and their concentration ratios. Beyond this information, we can also derive the conformational flexibility of these targets—the capacity of a biomolecule to undergo subtle conformational changes—from the distribution. To quantify this conformational flexibility, we fitted the $\Delta I/I_0$ distribution using a Gaussian function and calculated the full width at half maximum (FWHM) of the fitted curve. We use FWHM as a simple metric of conformational heterogeneity. A narrow FWHM indicates that most translocation events generate similar current amplitudes, consistent with a relatively rigid or compact conformation and a uniform translocation pathway. In contrast, a broad FWHM reflects a wide spread of current levels, as expected for a more flexible or heterogeneous ensemble that samples multiple conformations during translocation.

Fig. 6a illustrates the $\Delta I/I_0$ distribution and fitted curves for 7CE0 fragments measured at five varying voltages (150–500 mV) in a 1 M KCl concentration environment. Notably, the width of the $\Delta I/I_0$ distribution decreases significantly as the voltage increases from 150 mV to 500 mV. In contrast, at a lower concentration of 0.5 M (Fig. 6b), the distribution width increases markedly with elevated voltages. Fig. 6c

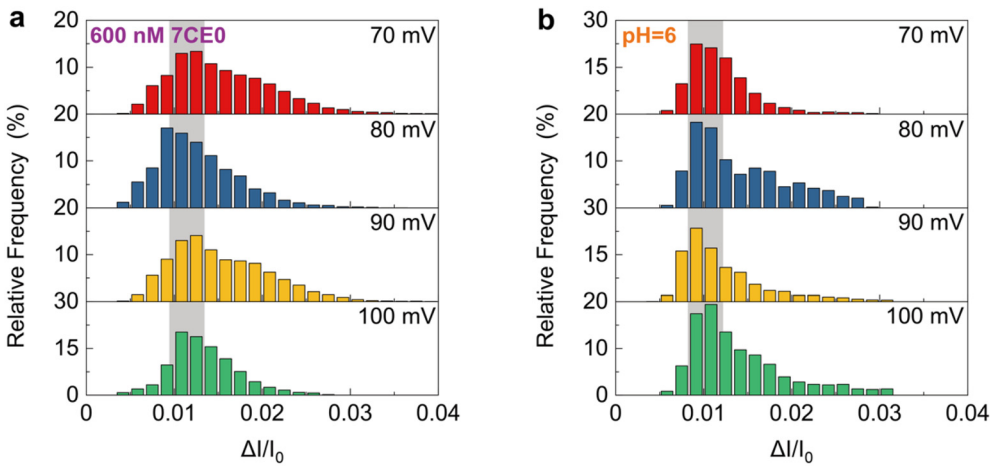

Fig. 5 Conformational spectra of the 7CE0 fragment under varying conditions. The nanopore diameter is 20 nm. (a) The distribution of $\Delta I/I_0$ values at a concentration of 600 nM across four applied voltages (70, 80, 90, and 100 mV). (b) The distribution of $\Delta I/I_0$ values at solution pH 6 across four applied voltages (70, 80, 90, and 100 mV). The number of events, *N*, for each condition is 1000.

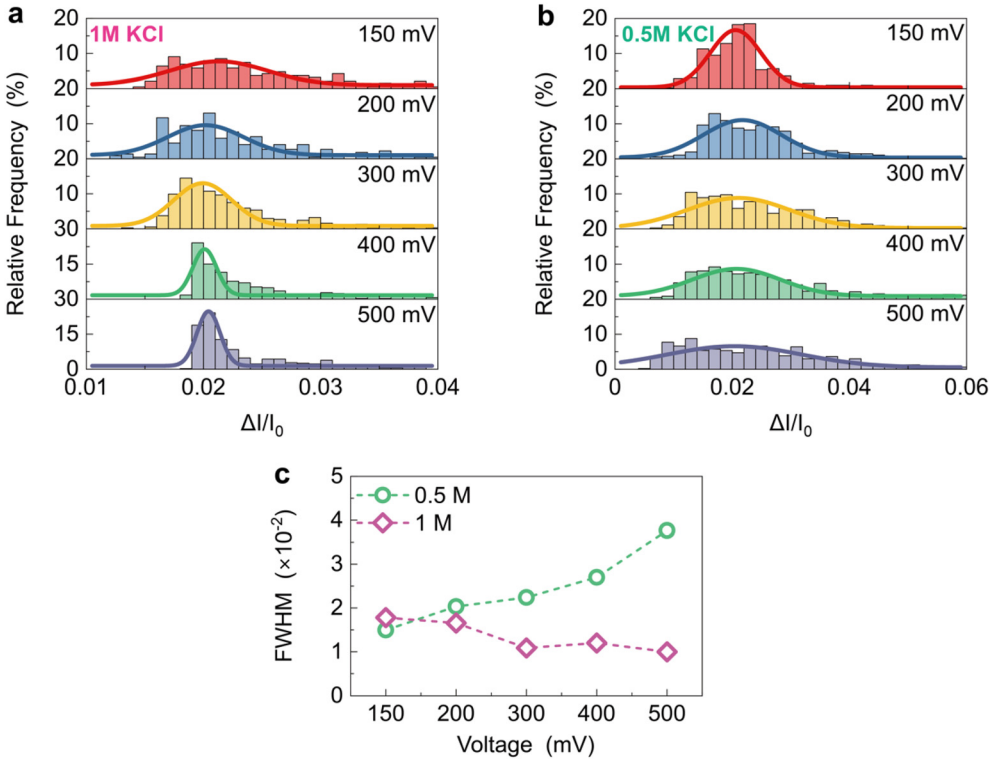

Fig. 6 Conformational spectra of 7CE0 fragments under varying voltages and ionic strengths. (a) The $\Delta I/I_0$ distribution and fitted Gaussian curves for 7CE0 fragments measured across five voltages (150–500 mV) in a 1 M KCl concentration. (b) The $\Delta I/I_0$ distribution and fitted Gaussian curves at a lower ionic strength of 0.5 M KCl. The number of events, *N*, for each condition is 1000. (c) The FWHM values plotted against voltage for both ionic strengths indicate distinct trends: at 1 M, the FWHM increases with voltage, while at 0.5 M, the FWHM decreases.

plots the FWHM as a function of voltage for both 1 M and 0.5 M concentrations. The FWHM values for the two ionic strengths exhibit distinct trends with increasing voltages; at high concentration, the FWHM increases, while at low concentration, it decreases.

These results indicate that the conformational flexibility of the 7CE0 fragment is strongly influenced by both voltage and ionic strength. We propose that at higher ionic strengths (1 M), the charges of the 7CE0 fragments are effectively screened, thereby reducing interactions among residues. As the driving forces (voltage) are increased, the fragments undergo more uniform and rapid translocation across the nanopore, resulting in a narrower FWHM.[39] Conversely, at lower ionic strength (0.5 M), the 7CE0 fragments experience reduced screening by ions, leading to increased conformational fluctuations. Under elevated voltages, the local electric forces acting on the residues may interact differently, further promoting these fluctuations. Consequently, the FWHM in this scenario increases with the applied voltage.

On the other hand, protein stability against the conformational flexibility is a key for their proper function and activity. Nanopore microscopy offers a way to probe the stability of proteins including their fragments under various surrounding artificial environments, which is crucial for proteomics and understanding biological protein-assisted processes.

Concluding remarks

In conclusion, our nanopore microscopy approach has provided insights into the conformational dynamics of SARS-CoV-2 N protein fragments, demonstrating the potential of single-molecule sensing techniques in probing protein domain behavior. By systematically exploring the translocation characteristics of 50-residue fragments from the N-terminal and C-terminal domains under varying voltage conditions, we have revealed dynamic transitions, particularly in the C-terminal domain fragment, which exhibits voltage-dependent dimerization and dissociation behaviors. The observed phenomenon of electric field-induced conformational changes not only provides understanding of protein fragment interactions but also highlights the nanopore platform's capacity to detect molecular transition with high sensitivity. The ability to resolve and quantify CTD monomer–dimer equilibria at the single-molecule level suggests potential applications in both antiviral drug discovery and diagnostics. In a therapeutic context, the CTD dimer interface represents a target for small molecules or peptides designed to either disrupt or stabilize this interaction, thereby perturbing downstream assembly or replication processes that depend on CTD oligomerization. From a diagnostic standpoint, the distinct blockade signatures of CTD monomers and dimers provide a direct readout of oli-

gomeric state that could be exploited to screen for modulators of CTD self-association or to develop nanopore-based assays for sensitive detection of viral proteins and their conformational/oligomeric changes in response to candidate antivirals. Future research should focus on extending this methodology to investigate other viral proteins, exploring the generalizability of these voltage-dependent conformational dynamics across diverse protein systems and potentially developing more sophisticated single-molecule sensing approaches for molecular characterization.

Methods and materials

Nanopore fabrication

We employed a well-established MEMS protocol to fabricate the nanopore chip wafer (Fig. S1 and S2). First, we grew a 1 μm SiO_2 layer on a 220 μm-thick silicon substrate *via* thermal oxidation, followed by the deposition of a 100 nm Si_3N_4 film through low-pressure chemical vapor deposition (LPCVD). We then patterned a 2.5 μm-diameter region on the Si_3N_4 surface by ultraviolet (UV) lithography and reactive ion etching (RIE), thinning the film from 100 nm to 20 nm.[40] Next, we used lithography on the wafer's reverse side to define a square etch window, which facilitated the selective removal of the silicon substrate by potassium hydroxide (KOH) wet etching. A subsequent buffered oxide etch (BOE) step removed the underlying SiO_2, thereby revealing a free-standing Si_3N_4 membrane. Before nanopore fabrication, we used Focus Ion Beam (FIB) to thin the membrane by approximately 10 nm with an eventual 10 nm thickness. Representative optical and scanning electron microscopy images of this membrane are shown in Fig. S3. The detailed protocol is provided in SI Note S1.

We fabricated the nanopore in the thin Si_3N_4 membrane, focusing on the circular etched region, by employing the controlled dielectric breakdown (CBD) technique.[41] Details are provided in SI Note S2. Briefly, we applied a high electric field across the membrane until it reached a threshold voltage, producing a stable, precisely localized pore. Specifically, we clamped the Si_3N_4 chip between two reservoirs filled with 1 M KCl, each equipped with an Ag/AgCl electrode, and used a computer-controlled source meter (Keithley 2612A, Keithley Instruments, Cleveland, USA) to apply voltage pulses at 25 Hz while simultaneously recording the ionic current to monitor pore formation.

Fig. S4c shows the resulting *I–V* curves obtained under 1 M KCl. We calculated the effective nanopore diameter from the measured ionic conductance (G_{pore}) using eqn (1). The nanopore diameter D can be calculated from G_{pore} as below,

$$D = \frac{G_{pore}}{2\kappa}\left(1 + \sqrt{1 + \frac{16\kappa l}{\pi G_{pore}}}\right) \quad (1)$$

where κ is the bulk ion conductivity of the solution (for 1 M KCl solution, κ = 11 S m^{-1} at temperature 25 °C and pH 7.0), and l is the nanopore length (*i.e.*, the Si_3N_4 membrane thickness). We modulated the nanopore diameter by controlling the voltage (Fig. S5).

Nanopore measurement

Before measurement, we immersed each single-nanopore chip in a piranha solution (3 : 1 H_2SO_4/H_2O_2) at 120 °C for 30 minutes to remove organic contaminants, followed by three rinses with deionized (DI) water. We stored the cleaned chips in DI water to preserve their hydrophilic surfaces. For measurements, we clamped each chip between two silicone elastomer gaskets attached to the entrance of a home-made polymethylmethacrylate (PMMA) flow cell, placing two Ag/AgCl electrodes, prepared by oxidizing silver wires in a 10% NaClO solution, in the *cis* and *trans* reservoirs to establish an electric circuit across the nanopore. Inside a dark Faraday cage, we used a resistive feedback amplifier (Axon MultiClamp 200B, Molecular Devices, CA, USA) to record the ionic current in voltage-clamp mode,[37] with current signals digitized at a 250 kHz sampling rate (Axon Digidata 1550A, Molecular Devices, CA, USA) and filtered at 10 kHz. Data acquisition was managed with pClamp 10 software (Molecular Devices, CA, USA). We conducted a bias sweep from −500 mV to +500 mV in 100 mV increments to obtain *I–V* curves. Ionic current rectification was examined to check whether the nanopore is symmetric.[42,43] After each set of experiments, we triple-rinsed both the flow cell and the chip with DI water before introducing the next solution. Recorded raw current traces are shown in Fig. S6.

Reagents and sample preparation

The experiments used the following commercial reagents: 7CE0 protein fragment (sequence: AAEASKKPRQKRTATKAYNVTQAFGRRGPEQTQGNFGDQELIRQGTDYKH, Sangon Biotech, Shanghai, China), 7CDZ protein fragment (sequence: SWFTALTQHGKEDLKFPRGQGVPINTNSSPDDQIGYYRRATRRIRGGDGK, Sangon Biotech, Shanghai, China), Tris-HCl buffer solution (Solarbio, Catalog number T1150-100), potassium chloride of ≥99% purity for molecular biology (Sinopharm, Catalog number 7447-40-7). Solutions and buffers for nanopore measurements, prepared with these reagents, were filtered twice using 0.22 μm Millipore syringe filters (MF-Millipore™, Sigma-Aldrich, catalog number GSWP02500). For most experiments, unless otherwise specified, we prepared the protein fragments in 10 mM Tris-HCl (pH 8) with 1 M KCl with gentle vortexing and spinning. No incubation was performed for both protein fragments. The time between sample preparation and nanopore measurement was around 15 min.

Molecular dynamics simulations

We performed all molecular dynamics simulations in NAMD,[44] and we conducted modeling, visualization, and analysis using Visual Molecular Dynamics (VMD).[45] In the simulation model, we fabricated the nanopore by removing Si and N atoms that satisfy the $x^2 + y^2 < (d/2)^2$ in the center of a silicon nitride (SiN) membrane.[46] We modified the nanopore's surface charge density (−0.05 C m^{-2}) by assigning the appropriate charge to the Si and N atoms.[47] We applied periodic boundary conditions along the x and y directions of the model. We employed the TIP3P model[48] for water molecules and adopted the CHARMM36[49] force field to describe atomic interactions, using a 1.2 nm cut-off distance

for non-bonded interactions. To facilitate peptide capture and reduce computational cost, we initially located the first amino acid 10 Å on the left side of the nanopore center. Using the Solvate plugin in VMD, we hydrated the system with water molecules, resulting in a final model of roughly 80 400 atoms. To maintain structural integrity, we imposed a harmonic restraint of 10.0 kcal mol^{-1} $Å^{-2}$ on the SiN membrane and another 1.0 kcal mol^{-1} $Å^{-2}$ restraint on the protein fragments to prevent it from exiting the pore during minimization and equilibration. Using NPT ensemble conditions, we maintained pressure at 1 atm along the *z*-axis dimension using the Nose–Hoover Langevin piston method. After 0.1 ns of conjugate gradient minimization, we equilibrated the system for 5 ns at constant pressure and temperature. We then conducted production simulations in NVT for 100 ns in the presence of an applied electric field to drive protein fragment translocation through the pore.

Author contributions

Dapeng Chen: methodology, investigation, validation, writing – original draft. Fei Zheng: conceptualization, formal analysis, writing – original draft. Guangle Qin: investigation. Lichun Zou & Chaofan Ma: formal analysis, investigation. Wei Liu: investigation. Haiyan Wang: conceptualization, methodology, resources, supervision. Jingjie Sha: investigation, funding acquisition, writing – review & editing, supervision.

Conflicts of interest

The authors declare no financial interests/personal relationships which may be considered as potential competing interests.

Data availability

The datasets generated and analyzed during this study are available from the corresponding author upon reasonable request. All relevant data supporting the findings of this study are included in the manuscript and its supplementary information (SI). This Supporting Information contains detailed methods for nanopore and chip fabrication, additional current traces and density plots, and molecular dynamics-based volume and interaction analyses. See DOI: https://doi.org/10.1039/d5an01140j.

Additional raw data files, analysis code, and protocols can also be made available to interested researchers upon request.

Acknowledgements

F. Z. and J. S. acknowledges funding from National Natural Science Foundation of China (52075099, 52361145851) and the Big Data Computing Center of Southeast University for computing resources. W. L. acknowledges funding from China Scholarship Council (202306090129).

References

1 W. Zheng, Q. Wuyun, Y. Li, *et al.*, Deep-Learning-Based Single-Domain and Multidomain Protein Structure Prediction with D-I-TASSER, *Nat. Biotechnol.*, 2025, 1–13.
2 T. Ji, P. Ge, S. Zhang, *et al.*, Remote on–off Switching of Protein Activity by Intrinsically Disordered Region, *Nat. Struct. Mol. Biol.*, 2025, 1–11.
3 R. Duran-Romaña, B. Houben, P. F. Migens, *et al.*, Native Fold Delay and Its Implications for Co-Translational Chaperone Binding and Protein Aggregation, *Nat. Commun.*, 2025, **16**(1), 1673.
4 N. Woolger, A. Bournazos, R. A. Sophocleous, *et al.*, Limited Proteolysis as a Tool to Probe the Tertiary Conformation of Dysferlin and Structural Consequences of Patient Missense Variant L344P, *J. Biol. Chem.*, 2017, **292**(45), 18577–18591.
5 H. Lu, Z. Zhu, L. Fields, *et al.*, Mass Spectrometry Structural Proteomics Enabled by Limited Proteolysis and Cross-Linking, *Mass Spectrom. Rev.*, 2024, DOI: 10.1002/mas.21908.
6 J.-G. Wang, R.-J. Yu, X. Hua, *et al.*, Pore Confined Time-of-Flight Secondary Ion Electrochemical Mass Spectrometry, *Chem. Soc. Rev.*, 2023, **52**(8), 2596–2616.
7 Y. Hu, K. Cheng, L. He, *et al.*, NMR-Based Methods for Protein Analysis, *Anal. Chem.*, 2021, **93**(4), 1866–1879.
8 R. Szabo, C. Nagy and A. Gaspar, Direct Injection Electrospray Ionization Mass Spectrometry (ESI-MS) Analysis of Proteins with High Matrix Content:Utilizing Taylor–Aris Dispersion, *Angew. Chem., Int. Ed.*, 2024, **63**(15), e202318225.
9 X. R. Liu, M. M. Zhang and M. L. Gross, Mass Spectrometry-Based Protein Footprinting for Higher-Order Structure Analysis: Fundamentals and Applications, *Chem. Rev.*, 2020, **120**(10), 4355–4454.
10 Y.-D. Yin, Y.-W. Zhang, X.-T. Song, *et al.*, Native Globular Ferritin Nanopore Sensor, *Nat. Commun.*, 2025, **16**(1), 5268.
11 Y.-L. Ying, Z.-L. Hu, S. Zhang, *et al.*, Nanopore-Based Technologies beyond DNA Sequencing, *Nat. Nanotechnol.*, 2022, **17**(11), 1136–1146.
12 W. Liu, Q. Zhu, C.-N. Yang, *et al.*, Single-Molecule Sensing inside Stereo- and Regio-Defined Hetero-Nanopores, *Nat. Nanotechnol.*, 2024, 1–9.
13 R. Hu, R. Zhu, G. Wei, *et al.*, Solid-State Quad-Nanopore Array for High-Resolution Single-Molecule Analysis and Discrimination, *Adv. Mater.*, 2023, **35**(24), 2211399.
14 Y. Lin, Y.-L. Ying, X. Shi, *et al.*, Direct Sensing of Cancer Biomarkers in Clinical Samples with a Designed Nanopore, *Chem. Commun.*, 2017, **53**(84), 11564–11567.
15 Q. Li, Y.-L. Ying, S.-C. Liu, *et al.*, Detection of Single Proteins with a General Nanopore Sensor, *ACS Sens.*, 2019, **4**(5), 1185–1189.
16 F. Zheng, H. Li, J. Yang, *et al.*, Improving Macromolecule Crowding Configurations in Nanopores for Protein Sensing, *Chem. Commun.*, 2024, **60**(95), 14097–14100.
17 Y. Li, Y. Yang, C. Zhong, *et al.*, Highly Sensitive Detection of T790 M with a Three-Level Characteristic Current by

Thymine–Hg(II)–Thymine in the α-Hemolysin Nanopore, *Anal. Chem.*, 2024, **96**(8), 3587–3592.
18 F. Zheng, M. Alawami, J. Zhu, *et al.*, DNA Carrier-Assisted Molecular Ping-Pong in an Asymmetric Nanopore, *Nano Lett.*, 2023, **23**(23), 11145–11151.
19 C. Ma, F. Zheng, W. Xu, *et al.*, Surface Roughness Effects on Confined Nanoscale Transport of Ions and Biomolecules, *Small Methods*, 2024, **8**(9), 2301485.
20 F. Zheng, A. Suma, C. Maffeo, *et al.*, Torsion-Driven Plectoneme Formation During Nanopore Translocation of DNA Polymers, *Phys. Rev. X*, 2025, **15**(3), 031041.
21 M.-Y. Li, J. Jiang, J.-G. Li, *et al.*, Nanopore Approaches for Single-Molecule Temporal Omics: Promises and Challenges, *Nat. Methods*, 2024, 1–13.
22 F. Zheng and Q. Han, Distinct DNA Conformations during Forward and Backward Translocations through a Conical Nanopore, *Analyst*, 2024, **149**(20), 5131–5138.
23 Z.-Q. Zhou, S.-C. Liu, J. Wang, *et al.*, Exploring a Solid-State Nanopore Approach for Single-Molecule Protein Detection from Single Cells, *Chem. Sci.*, 2025, **16**(19), 8501–8508.
24 R. Hu, W. Lu, G. Wei, *et al.*, Label-Free Detection and Translocation Dynamics Study of Single-Molecule Herceptin Using Solid-State Nanopores, *Adv. Mater. Technol.*, 2022, **7**(12), 2200018.
25 W. Liu, J. Andersson, J. Järlebark, *et al.*, The Electric Field in Solid State Nanopores Causes Dissociation of Strong Biomolecular Interactions, *Nano Lett.*, 2025, **25**(24), 9654–9661.
26 Z. Wang, R. Hu, R. Zhu, *et al.*, Metal–Organic Cage as Single-Molecule Carrier for Solid-State Nanopore Analysis, *Small Methods*, 2022, **6**(11), 2200743.
27 S.-C. Liu, Y.-L. Ying, W.-H. Li, *et al.*, Snapshotting the Transient Conformations and Tracing the Multiple Pathways of Single Peptide Folding Using a Solid-State Nanopore, *Chem. Sci.*, 2021, **12**(9), 3282–3289.
28 R. Hu, C. Liu, W. Lu, *et al.*, Probing the Effect of Ubiquitinated Histone on Mononucleosomes by Translocation Dynamics Study through Solid-State Nanopores, *Nano Lett.*, 2022, **22**(3), 888–895.
29 H. Chen, Y. Cui, X. Han, *et al.*, Liquid–Liquid Phase Separation by SARS-CoV-2 Nucleocapsid Protein and RNA, *Cell Res.*, 2020, **30**(12), 1143–1145.
30 Z.-Q. Zheng, S.-Y. Wang, Z.-S. Xu, *et al.*, SARS-CoV-2 Nucleocapsid Protein Impairs Stress Granule Formation to Promote Viral Replication, *Cell Discovery*, 2021, **7**(1), 38.
31 Y. Peng, N. Du, Y. Lei, *et al.*, Structures of the SARS–CoV–2 Nucleocapsid and Their Perspectives for Drug Design, *EMBO J.*, 2020, **39**(20), e105938.
32 R. Zeng, M. Qiu, Q. Wan, *et al.*, Smartphone-Based Electrochemical Immunoassay for Point-of-Care Detection of SARS-CoV-2 Nucleocapsid Protein, *Anal. Chem.*, 2022, **94**(43), 15155–15161.
33 H. Zhao, D. Wu, S. A. Hassan, *et al.*, A Conserved Oligomerization Domain in the Disordered Linker of Coronavirus Nucleocapsid Proteins, *Sci. Adv.*, 2023, **9**(14), eadg6473.
34 W. Wu, Y. Cheng, H. Zhou, *et al.*, The SARS-CoV-2 Nucleocapsid Protein: Its Role in the Viral Life Cycle, Structure and Functions, and Use as a Potential Target in the Development of Vaccines and Diagnostics, *Virol. J.*, 2023, **20**(1), 6.
35 W. Liu, Y. Zhang, Z. Gu, *et al.*, Structure Design of Silicon-Based Nanopore Chips for Noise Reduction, *IEEE Sens. J.*, 2024, **24**(3), 2405–2412.
36 W. Liu, F. Zheng, C. Ma, *et al.*, Single-Digit Nanobubble Sensing via Nanopore Technology, *Anal. Chem.*, 2024, **96**(23), 9544–9550.
37 F. Zheng, Y. Tao, W. Xu, *et al.*, Detection of DNA Translocations in a Nanopore Series Circuit Using a Current Clamp, *Phys. Chem. Chem. Phys.*, 2023, **25**(15), 10440–10446.
38 K. L. Zapadka, F. J. Becher, A. L. Gomes dos Santos, *et al.*, Factors Affecting the Physical Stability (Aggregation) of Peptide Therapeutics, *Interface Focus*, 2017, **7**(6), 20170030.
39 J.-G. Li, M.-Y. Li, X.-Y. Li, *et al.*, Full Width at Half Maximum of Nanopore Current Blockage Controlled by a Single-Biomolecule Interface, *Langmuir*, 2022, **38**(3), 1188–1193.
40 W. Liu, J. Shang, F. Zheng, *et al.*, A Droplet Memristor with Ionic Liquid-Electrolyte Meniscus, *Chem. Eng. J.*, 2025, **504**, 158948.
41 J. P. Fried, J. L. Swett, B. P. Nadappuram, *et al.*, Understanding Electrical Conduction and Nanopore Formation During Controlled Breakdown, *Small*, 2021, **17**(37), 2102543.
42 F. Zheng, H. Li, J. Yang, *et al.*, A Switchable and Facile Ionic Diode Modulated by Polyethylene Glycol, *Chem. Commun.*, 2024, **60**(97), 14471–14474.
43 F. Zheng, H. Li, J. Yang, *et al.*, Modulation of Ion Transport in Nanopores Using Polyethylene Glycol, *Langmuir*, 2024, **40**(50), 26742–26750.
44 J. C. Phillips, R. Braun, W. Wang, *et al.*, Scalable Molecular Dynamics with NAMD, *J. Comput. Chem.*, 2005, **26**(16), 1781–1802.
45 W. Humphrey, A. Dalke and K. Schulten, VMD: Visual Molecular Dynamics, *J. Mol. Graphics*, 1996, **14**(1), 33–38.
46 F. Zheng, Y. Wu and H. Yi, Exploring the Onset Field Strength of Nanoscale Electrospray: A Detailed Investigation, *Chem. Phys. Lett.*, 2024, **854**, 141566.
47 F. Zheng, S. Zhang, J. Mo, *et al.*, Ion Concentration Effect on Nanoscale Electrospray Modes, *Small*, 2020, **16**(24), 2000397.
48 F. Chen and P. E. Smith, Simulated Surface Tensions of Common Water Models, *J. Chem. Phys.*, 2007, **126**(22), 221101.
49 J. Lucker, M. Kio and J. B. Klauda, Expanding the CHARMM36 United Atom Chain Model for the Inclusion of Sphingolipids, *J. Phys. Chem. B*, 2024, **128**(18), 4428–4439.

